Multistability and Gibbs entropy in the planar dissipative spin-orbit problem

Vitor M. de Oliveira

Abstract In this work, we numerically investigate and visually illustrate the dynamical properties of the dissipative spin-orbit problem such as the co-existence of multiple periodic and quasi-periodic attractors, and the complexity of the corresponding basins of attraction. Our model is composed by a tri-axial satellite (planet) orbiting a planet (star) in a fixed Keplerian orbit with zero obliquity. A dissipative tidal torque that is proportional to its rotational angular velocity is assumed to be acting on the satellite. We use Hyperion as a toy model to characterize the methodology used, since this system has a very rich conservative dynamical scenario, and we later apply our methodology to the Moon and Mercury. Our results show that the basins of attraction may possess an intricate structure in all cases which changes with the orbital eccentricity, and that the Gibbs entropy is a good measure on how dominant one basin is over the others in the phase space.

Keywords Spin-orbit coupling · Multistability · Gibbs entropy

1 Introduction

Many natural satellites in the Solar System, including the Moon, are observed in an orbital period similar to their rotational period. These bodies probably rotated much fast upon their formation and then went through a despinning process due to tidal interactions with their massive companions (MacDonald 1964; Kokubo and Ida 2007), until eventually ending up in a synchronous rotation. Since the seminal work by Darwin (1879), many authors have studied the rotational dynamics of orbiting bodies under the ef-

Instituto de Matemática e Estatística, Universidade de São Paulo, 05508-090 São Paulo/SP, Brazil, and
CFisUC, Departamento de Física, Universidade de Coimbra, 3004-516 Coimbra, Portugal
E-mail: vitormo@ime.usp.br | vitor.m.oliveira@uc.pt

fect of tidal forces, such as Efroimsky (2012); Ferraz-Mello (2013); Correia et al. (2014); Ragazzo and Ruiz (2017); Correia and Delisle (2019). Such phenomenon mainly affects the motion of orbiting bodies that are bigger or closer to the central body (Murray and Dermott 1999), but it can also impact the evolution of small bodies (Goldreich and Re'em 2009).

The closest planet to the Sun, Mercury, is currently moving in a $3/2$ spin-orbit resonance, i.e., it takes the same amount of time to rotate around its spin axis thrice as it takes to revolve around the Sun twice. This discover by Pettengill and Dyce (1965) showed that the system can be locked into other configurations besides the synchronous one, which has lead to many works regarding the final state of tidally evolved systems. In particular, Goldreich and Peale (1966) derived an analytical probability for a planet or satellite to be captured into a spin-orbit resonance based on arguments about energy dissipation, while Henrard (1985) reinterpreted the probability of capture in terms of Adiabatic Invariant Theory. Later, Correia and Laskar (2004) showed that the chaotic evolution of Mercury's orbit could have driven its orbital eccentricity high enough during the planet's history so that the probability of it ending up in its current state is actually higher than previously thought.

From a Dynamical Systems perspective, we can interpret the probability of being captured by a resonance as the probability of a random trajectory converging to a given final state in the phase space. In a system with multi-stability, i.e., many co-existing attractors, such concept can be related to the size of the basin of attraction associated with each attractor (see Celletti and Chierchia 2008). Here, we are interested in visually illustrating and also quantifying the complexity of the basins of attraction in the spin-orbit problem. To carry on with this investigation, we choose a low-dimensional model of the problem which assumes that the orbiting body follows a Keplerian orbit with fixed parameters and rotates perpendicularly to the orbit plane. We then determine the basins of attraction of the main resonances, and we measure their respective sizes and entropy. Our results highlight the rich dynamical scenarios that may emerge from such a system. We depict the intricate structure formed by the basins of attraction in the spin-orbit problem, and we evaluate how dominating one of the attractors is over the others via the Gibbs entropy, which are the main contributions of this work.

This paper is organized as follows. In Sec. 2 we present the equations of motion for our physical model. Later, in Sec. 3 we briefly expose the main ideas regarding the Gibbs entropy in our context. The dynamical analyses for Hyperion, the Moon and Mercury are presented in Secs. 4 and 5. Finally, in Sec. 6 we give some general remarks and state our conclusions.
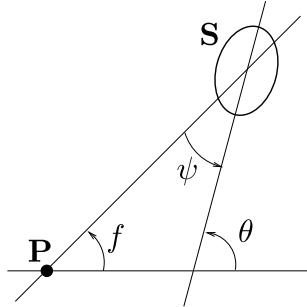
2 Physical model

Our physical model consists in an orbiting body that revolves around a central body with the following considerations: the orbit is given by a fixed Keplerian ellipse with eccentricity e, semi-major axis a and instantaneous ra-

dius r; the central body is a point particle whilst the orbiting body is a triaxial almost-rigid rotating body with principal moments of inertia $I_1 < I_2 < I_3$; the orbiting body's spin-axis is parallel to I_3 and perpendicular to the orbit plane; and the only forces acting on the orbiting body are due to the gravitational field generated by the central body.

We also consider that the central body rises a tide on the orbiting body. The time lag τ between the distortion of the body and the tide-raising potential is assumed to be constant (Singer 1968; Mignard 1979), which leads to a phase lag, and consequently a dissipation function, that is linearly dependent on the relative angular velocity $\dot{\psi}$ (Peale 2005; Efroimsky and Lainey 2007).

The position of the orbiting body along its trajectory may be determined by the true anomaly f, and its rotation may be evaluated by the angle θ between the axis along I_1 (largest physical axis) and a coordinate axis fixed in inertial space, which we take to intersect both the central body and the point of periapsis. We illustrate the system in Fig. 1.

Fig. 1: Schematic of the system. The satellite **S** orbits the planet **P** following a Keplerian orbit. f stands for the true anomaly and θ for the rotation angle.

With the aforementioned considerations, our equation of motion is

$$I_3\ddot{\theta} = -\frac{3}{2}(I_2 - I_1)\frac{Gm_P}{r^3}\sin 2\psi - 3k_2\frac{Gm_P^2 R^5}{r^6}\tau\dot{\psi}, \qquad (1)$$

where G is the gravitational constant, m_P is the planet's mass and $\psi = \theta - f$. The first term on the right-hand side of Eq. (1) is the gravitational torque, and the second term is the dissipative tidal torque, where k_2 is the Love number and R is the satellite's radius.

By rearranging the terms in Eq. (1) and denoting the equatorial oblateness by $\gamma = 3(I_2 - I_1)/2I_3$, our equation of motion can be rewritten as

$$\ddot{\theta} = -\gamma\frac{Gm_P}{r^3}\sin 2(\theta - f) - K\big(L\dot{\theta} - N\big), \qquad (2)$$

with

$$L = \frac{a^6}{r^6} \qquad \text{and} \qquad N = \frac{a^8 n\sqrt{1 - e^2}}{r^8},$$

where n is the satellite's mean motion.

We are interested in spin-orbit resonances, solutions where the number of revolutions around the central body and the number of rotations around its spin-axis are commensurable. Following the definition in Celletti and Chierchia (2008), if T is the satellite's orbital period, a *spin-orbit resonance* (SOR) of type p/q is a solution for the system such that

$$\theta(t + Tq) = \theta(t) + 2\pi p \qquad \text{for all} \qquad t \in \mathbb{R},$$

for two relatively prime integers p, q with $q > 0$.

The spin-orbit resonances are, by definition, periodic orbits. For $K = 0$, Eq. (2) describes an one-and-a-half degree of freedom near integrable conservative system, with both γ and e as perturbation parameters. Therefore, the system can possess a mixed phase space, with the coexistence of regular and chaotic motion (Lichtenberg and Lieberman 1992). For $K > 0$, some spin-orbit resonances may become periodic attractors of the system, being the final state of a set of trajectories with positive measure. We call the set of initial conditions that converge in time to a given attractor the *basin of attraction* of said solution (Alligood et al. 2012). For certain parameters, Eq. (2) also has solutions where p/q is irrational. Such orbits form KAM curves in the conservative case and may become quasi-periodic attractors in the dissipative case (Celletti and Chierchia 2009).

In order to help us analyze the spin-orbit problem, we define a *stroboscopic map* $\mathbf{M}$ which acts on the system's phase space as $(\theta(t), \dot{\theta}(t)) \rightarrow (\theta(t+T), \dot{\theta}(t+T))$. With this definition, we reduce the three-dimensional continuous system to a two-dimensional autonomous discrete system. Note that the spin-orbit resonances are represented on $\mathbf{M}$ by periodic orbits with period q, while the quasi-periodic solutions are represented by one-dimensional curves.

The model presented in this Section is well established and was used to study spin-orbit coupling in many works. See, for example, Wisdom et al. (1984); Correia and Laskar (2004); Celletti and Chierchia (2008); Celletti and Lhotka (2014). The fact that it is a low-dimensional model gives us access to numerical tools that are capable of visually illustrating the dynamical properties of orbits in the phase space.

3 Entropy

The basin of attraction is the portion of the phase space where initial conditions lead to orbits that converge to the attractor. Hence the size of the basin of attraction can be interpreted as the probability of a random initial condition to belong in said basin. In multistable systems, multiple basins coexist and their basins compete for room in the phase space. In this situation, the individual basin sizes give the probability of a random initial condition to converge to a certain final state. Although very relevant, this information alone does not reflect how dynamically complex the phase space is. More specifically, it does not show how the phase space is divided among the basins.

In order to infer some information on that matter, we use the Gibbs entropy S, which is defined as (Gibbs 2010)

$$S = \sum_{i=1}^{N_A} p_i \ln \left(\frac{1}{p_i} \right),$$ (3)

where N_A is the number of attractors and p_i is the probability of a given orbit to belong to the basin of attraction of the i-th attractor.

The entropy S condenses in one number how heterogeneous the basin sizes are. It is maximum when all basins have the same size, i.e., $p_i = 1/N_A$ for every attractor. In this situation, we obtain

$$S_{max} = \ln N_A.$$

Hence, the entropy reflects how dominant an attractor is in the phase space in terms of its basin size, and it also takes into consideration the total number of attractors, expressed by its maximum value, which depends on the system parameters.
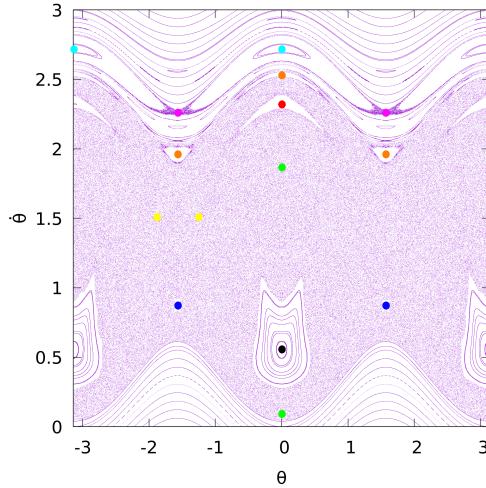
It is worth mentioning that an entropy called *basin entropy* was defined in (Daza et al. 2016) as a tool to assist in the classification of boundaries between the basins of attraction, which are related to the uncertainty in dynamical systems. This quantity was based on the Gibbs entropy and it was later shown that it was also related to dynamical and geometrical aspects such as uncertainty exponents and lacunarity (Daza et al. 2022).

As we are going to depict in the next sessions, the structure of the basin boundaries in the dissipative spin-orbit problem can be mostly perceived visually as riddled basins (see, for example, Alexander et al. 1992), where the unpredictability is maximum and the measure of uncertainty exponents do not give much information (Daza et al. 2022). Hence, the measure of the system's complexity here can be taken directly from the Gibbs entropy.

4 Hyperion

Hyperion is a moon of Saturn that is currently believed to be rotating chaotically (Wisdom et al. 1984; Wisdom 1987a). This natural satellite has a highly aspherical shape, being nearly twice as long as it is across, with physical parameters given by $e_{hyp} = 0.1$ and $\gamma_{hyp} = 0.396$ (Wisdom 1987b). In this section, we adopt these parameters in order to study the spin-orbit problem.

For all our simulations, we start the orbital motion of the satellite at *periapsis*, i.e., $f(t = 0) = 0$ and $r(t = 0) = a$, and we calculate $r(t)$ via Newton's equation. We also take $a = 1$ and $T = 2\pi$, which leads to $n = 1$ and $Gm_p = 1$. Numerical integration is carried out using an explicit embedded Runge-Kutta Prince-Dormand 8(9) scheme with adaptive step-size control (Galassi et al. 2001).
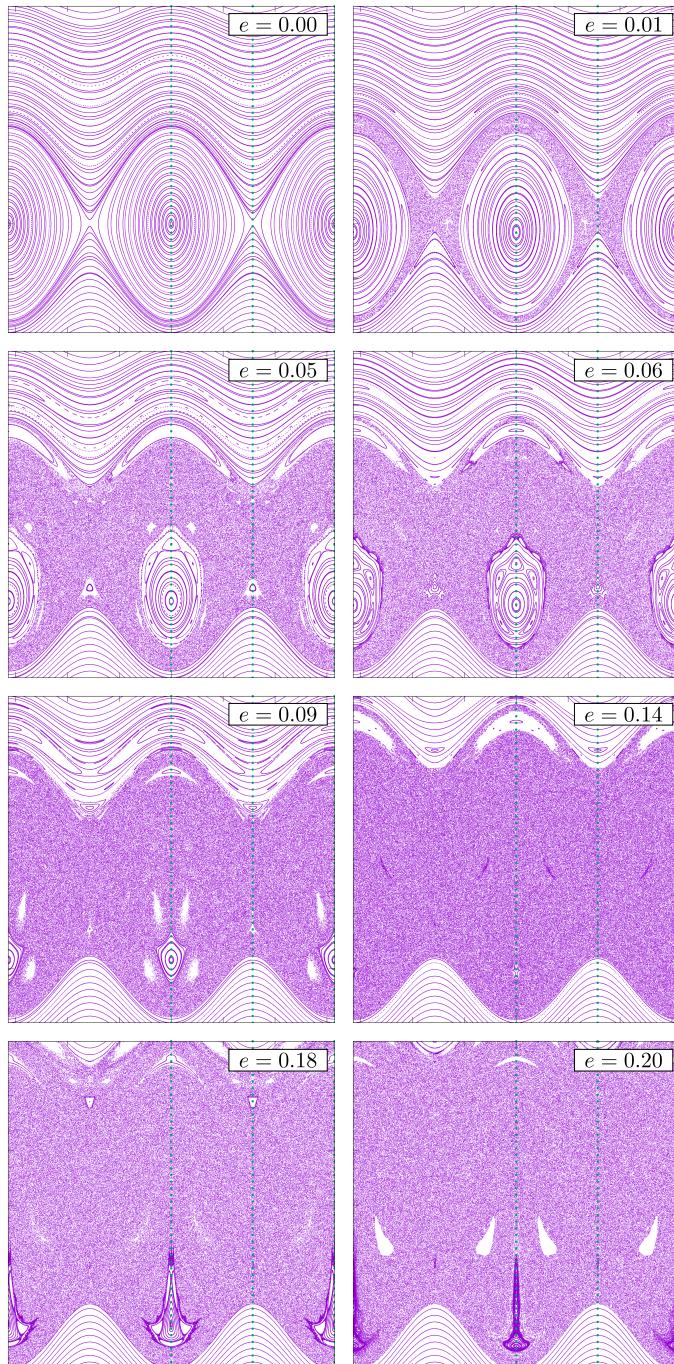
Fig. 2: Hyperion's phase space with main SORs. 1/1 stable (black), 2/1 stable (red), 1/2 stable (dark blue), 2/2 unstable (green), 3/2 unstable (yellow), 5/2 stable (light blue), 5/2 unstable (pink), and 9/4 stable (orange).

4.1 Conservative scenario

Let us first consider the case where Hyperion is treated as a rigid body and hence there is no tidal dissipation in the satellite's rotation. In this case, we have $K = 0$, and the gravitational torque is the only term present in Eq. (2). Figure 2 shows the system's phase space $\theta \times \dot{\theta}$ calculated on the stroboscopic map M. We can observe a typical near-integrable Hamiltonian system scenario, with regions of regular motion coexisting with chaos.

The location of a few low-order spin-orbit resonances are also marked in Fig. 2 by coloured points. We determine these periodic orbits to a high accuracy ($\sim 10^{-10}$) using a routine to select good candidates along with an iterative minimization procedure (see, for example, the Appendix of Raphaldini et al. 2020). For a SOR of type p/q, the value of q reflects the period of the orbit on $\mathbf{M}$, while p is the number of rotations measured outside the surface of section after q intersections.

Since in reality the physical parameters are not constant in time, it is important for us to understand how the system changes as we vary these. In Fig. 3, we present the phase space for different values of the orbital eccentricity e inside a given range. What we observe is the system going from a pendulum-like regular motion to a mixed phase space as the value is increased. During this process, some SORs bifurcate, changing stability, and regions of regular motion vary in size. For even larger values, we have the selected region of the phase space almost fully covered by chaotic orbits.
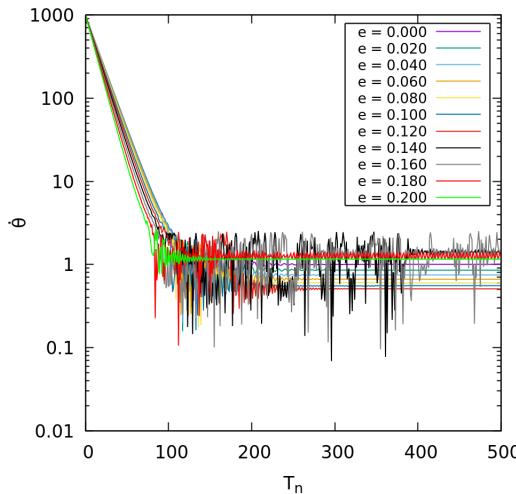
Fig. 3: Phase space for $\gamma = \gamma_{hyp}$, $K = 0$, and different values of e. The initial conditions chosen for these figures are marked by green dots.

4.2 Time series with tidal dissipation

When we consider Hyperion as an almost rigid body, tidal dissipation comes into effect and some of the spin-orbit resonances become attractors. However, as we showed in Fig. 3, the system's dynamical scenario vastly changes as we vary the eccentricity. In Fig. 4, the evolution of the angular velocity $\dot{\theta}$ is shown as a function of the number of orbital periods T_n (the unity of time in $\mathbf{M}$), for an initial condition given by $\theta(0) = 0.0$ and $\dot{\theta}(0) = 1000.0$ rad/s (i.e., Hyperion initially facing Saturn and rotating fast), and for different values of e.
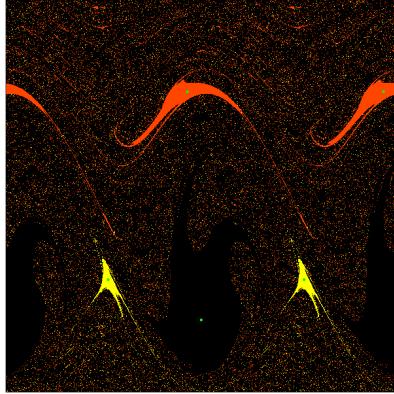
We choose a dissipation constant of $K = 10^{-2}$, a value which is high enough to allows us to observe the effects that tidal dissipation has on the system in a reasonable amount of simulation time, and low enough so that the interesting dynamical phenomena are not totally suppressed by the dissipation.

Fig. 4: Discrete-time series for the angular velocity $\dot{\theta}$ of a trajectory on $\mathbf{M}$ beginning at $\theta(0) = 0.0$ and $\dot{\theta}(0) = 1000.0$ rad/s, for $K = 10^{-2}$, $\gamma = \gamma_{hyp}$, and different values of e.

Two conclusions can be taken from Fig. 4. First, the discrete-time series is composed by three parts: an exponential decay, an erratic motion, and an asymptotic state corresponding to a resonance. Second, varying the value of the eccentricity affects the time series mostly in two manners: it changes the slope corresponding to the initial exponential decay, and it possibly modifies the trajectory's final state, i.e., to which SOR the trajectory eventually converges.

When dissipation is considered, the chaotic nature of the system translates as chaotic transients in the phase space. This can be seen in the erratic portion of the time series in Fig. 4. Hence, the system still presents sensitive dependence on initial conditions, i.e., initial conditions that are close together can lead to very different trajectories, which might converge to different SORs

Fig. 5: Basins of attraction for Hyperion with dissipation constant given by $K = 10^{-2}$. The color code corresponds to the following SORs: $1/1$ (black), $2/1$ (orange), and $1/2$ (yellow). The location for the SORs is marked with little green dots.
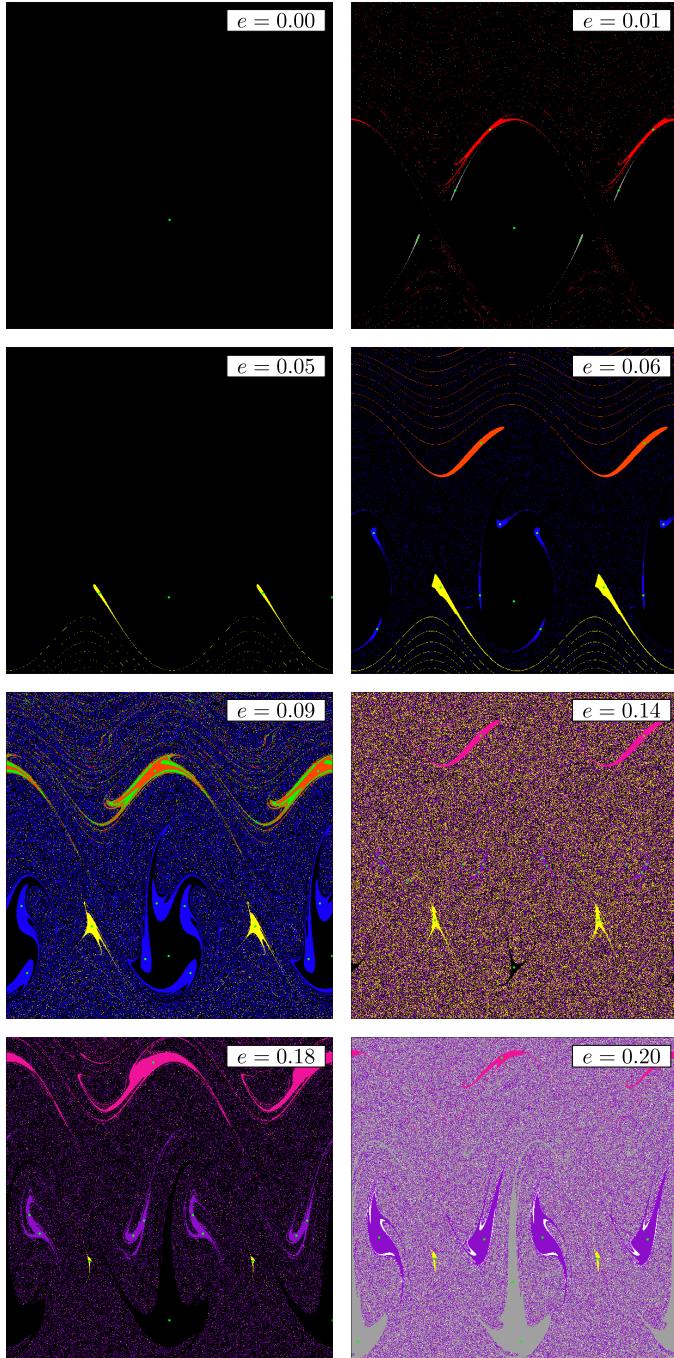
(see, for example, Ott 2002). Chaotic orbits can also mimic dynamical aspects of unstable periodic orbits inside the chaotic sea for a limited amount of time. With this, a trajectory on the phase space can become temporarily trapped around attractors during its chaotic transient.

Both dynamical aspects mentioned before, namely, sensitive dependence on initial conditions and temporary entrapment, are related to invariant manifolds of unstable periodic orbits (see, for example, de Oliveira et al. 2020). These geometrical structures permeate the phase space, bending and crossing each other, and rendering the system dynamics very complex. They also play an important role on the spin-resonance capture, since they form the boundaries of the basins of attraction.

4.3 Basins of attraction

In order to visually illustrate the basins of attraction, we selected a square grid of 600×600 initial conditions, evolved the equations of motion for each one and determined their final state. The results for Hyperion are shown in Fig. 5. For this system, there are three SORs, namely, $1/1$, $1/2$, and $2/1$, and it is possible to observe two aspects: the basin of the synchronous resonance dominates the phase space, and the boundaries between the basins are complex. The basin sizes, which are based on the number of points on the grid that compose each of them, are presented in Table 1.

In Fig. 6, we maintain the values for γ and K used in Fig. 5, and we calculate the basin of attraction of SORs with $p \leq 9$ and $q \leq 4$ for the same values of e as in Fig. 3. For $e = 0$, the $1/1$ SOR is the only resonance present and hence its basin of attraction (in black) fills the phase space. As the value for the orbital eccentricity is increased, other attractors appear along with their
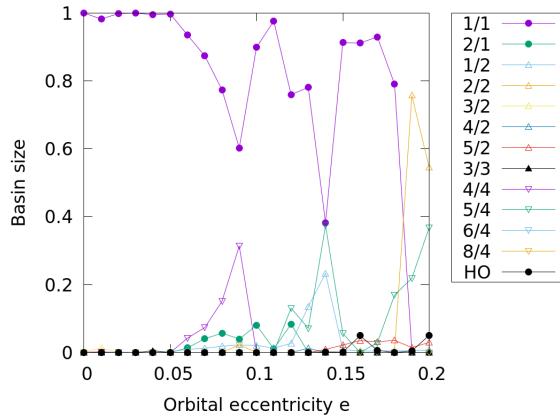
Fig. 6: Basins of attraction for $K = 10^{-2}$, $\gamma = \gamma_{hyp}$, and different values of e. The color code corresponds to the following SORs: 1/1 (black), 2/1 (orange), 1/2 (yellow), 2/2 (gray), 3/2 (red), 4/2 (dark-green), 5/2 (pink), 4/4 (blue), 5/4 (violet), and 8/4 (green). The basin of higher-order resonances is white, and the location for the SORs is marked with little green dots.

Table 1: Basin sizes and entropy for $e = e_{hyp}$, $\gamma = \gamma_{hyp}$, and $K = 10^{-2}$.

Basin size			Entropy
1/1	2/1	1/2	
89.94%	8.00%	2.06%	0.344

basins (multistability). The basins of attraction are notable intertwined with each other in the phase space, highlighting the complex dynamical scenario of the system. For $e = 0.2$, the synchronous resonance has bifurcated (period-doubling), giving origin to a 2/2 SOR (basin in blue). Note that the 2/2 SOR is different from the 1/1 SOR, since this solution only closes after the body fully rotates around itself two times, which takes two orbital periods.
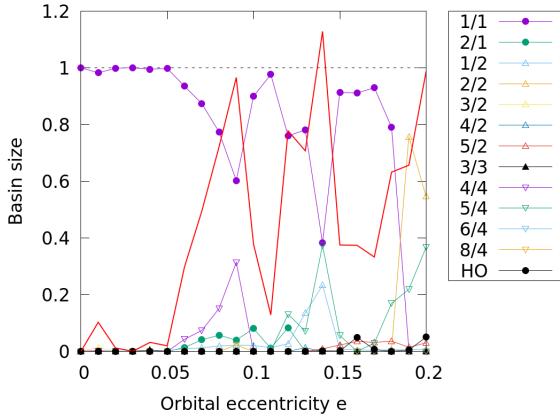
Here we are treating different attractors that correspond to a similar SOR as effectively the same attractor, since we can assume that they lead to the same physical outcome. For example, if the orbiting body is in the synchronous solution, it only shows the same side to the central body. However, there is another synchronous solution, where the orbiting body would always show its other side to the central body. If we were not to consider that these solutions were the same, the complexity of the system would increase since there would be more final states and, consequently, more basins of attraction.

Fig. 7: Size of the basins of attraction for $\gamma = \gamma_{hyp}$ and $K = 10^{-2}$. HO stands for higher-order SORs ($p > 9$ or $q > 4$).

In Fig. 7, we plot the size of the basins of attraction as a function of the eccentricity e. Here, we consider SORs with $p > 9$ or $q > 4$, higher-order (HO) resonances, as one single final state. As observed in Fig. 6, the basin size for the synchronous resonance dominates for lower values of eccentricity ($e \leq 0.05$). However, it competes for space with other basins as the eccentricity increases,

especially for $e = 0.09$ and $e = 0.14$, where the probability of a random trajectory to converge to the 1/1 spin-orbit resonance falls to approximately 0.6 and 0.4, respectively. For these parameters, the 4/4 SOR ($e = 0.09$), and the 5/4 and 1/2 SORs ($e = 0.14$) also become probable outcomes.

The entropy for the parameters used in Fig. 7 are presented in Fig. 8. The most striking result we observe is that the system's entropy is highly correlated to the basin size of the synchronous resonance. As the orbital eccentricity changes, the entropy varies and such variation inversely follows the tendency of the 1/1 SOR basin size, even when its value goes below 0.5 ($e = 0.14$). Therefore the complexity of the system depends on the basin size of the synchronous resonance when such solution is stable. For $e > 0.18$, the entropy starts to follow the 2/2 SOR. Hence in general the entropy acts in accordance to the basin size of the SOR with lowest order available.
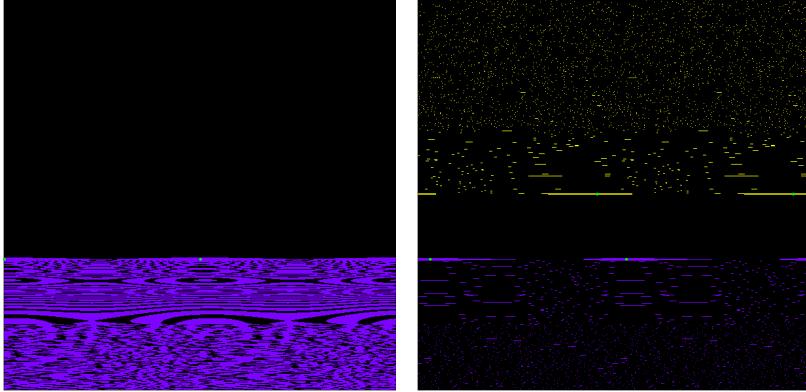

Fig. 8: Entropy (red curve) as a function of the orbital eccentricity alongside the basin sizes, for $\gamma = \gamma_{hyp}$ and $K = 10^{-2}$.

5 Moon & Mercury

We now proceed to the cases of the Moon and Mercury, meaning that we choose orbital eccentricities that correspond to those of these celestial bodies, namely $e_{Moon} = 0.0549$ and $e_{Mercury} = 0.2056$, and we set a constant parameter which is closer than the previous case to a real-life scenario but high enough so that numerical simulations can be carried out in a feasible amount of time, namely $K = 10^{-4}$. In both cases, we adopted an equatorial oblateness of $\gamma = 10^{-4}$.

In Fig. 9, we present the basins of attraction for the Moon (left) and Mercury (right). Here we set a fixed step size for the numerical integration scheme, and we calculated the basin of attraction on a square grid of 300×300 initial

conditions. In both cases, there exists quasi-periodic attractors, whose basin is shown in black. As was done for Hyperion regarding higher-order resonances, we do not differentiate between distinct quasi-periodic attractors and consider them to represent the same final state. The basin for the synchronous resonance is painted purple, while the one for the 3/2 SOR is painted yellow.
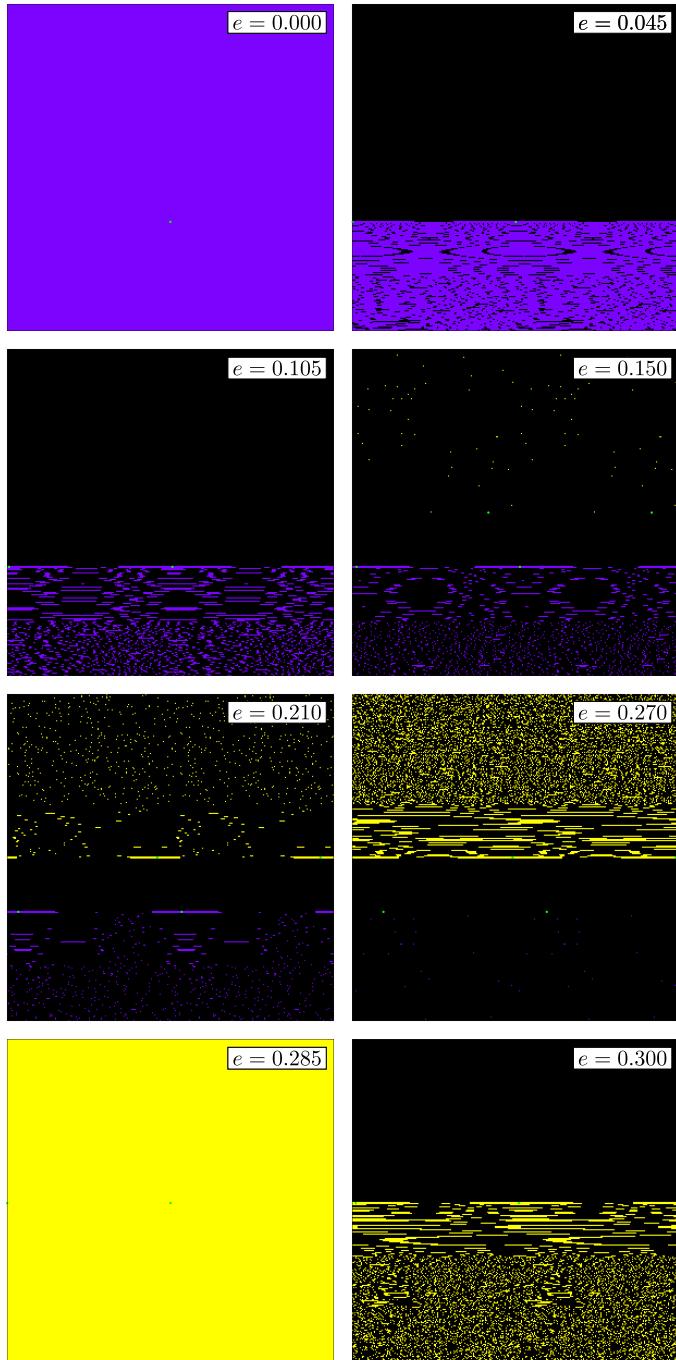

Fig. 9: Basins of attraction for (left) $e = e_{Moon}$ and (right) $e = e_{Mercury}$. Dissipation constant and equatorial oblateness are given by $K = 10^{-4}$ and $\gamma = 10^{-4}$, respectively. The color code corresponds to the following attractors: quasi-periodic (black), 1/1 (purple), and 3/2 (yellow). The location for the SORs is marked with little green dots.

The scenario for both the Moon and Mercury is quite different from Hyperion's (see Fig. 5). First, there is the presence of quasi-periodic attractors in the system. Second, the basin of attraction associated with the quasi-periodic attractor separates the other basins in the phase space. Hence, there is no basin boundary between the synchronous resonance and the 3/2 SOR for Mercury.

The compactness of the basins in Fig. 9 can be associated to the lower value of γ, where the system behaves more like a pendulum, and the lower value of K, where the system does not differ much from a conservative system. In this situation, the manifolds that separate the phase space are packed closely together, leading to a dynamical scenario different from the one observed for Hyperion.

While the Moon contains only the synchronous resonance besides the quasi-periodic attractor, Mercury also contains the 3/2 SOR. The associated basin sizes and entropy are shown in Tab. 2. Even though both situations present an intricate basin structure, the quasi-periodic attractor dominates the phase space for $e = e_{Mercury}$, and hence the entropy is smaller in comparison to the Moon, where the synchronous resonance fills a large area of the phase space.

In Fig. 10, we maintain $\gamma = 10^{-4}$ and $K = 10^{-4}$, and we depict the basins of attraction for different values of e. As before, the basin of the quasi-periodic solutions are shown in black, while the basin for the synchronous
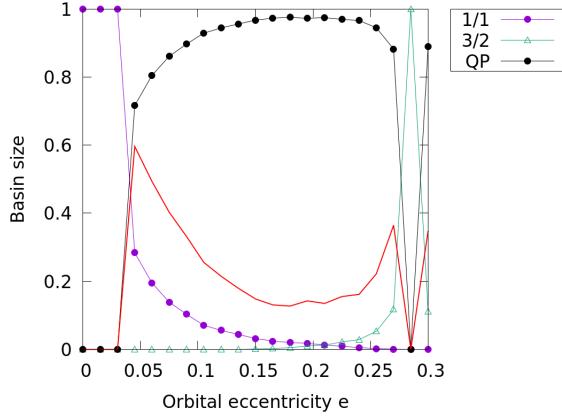
Fig. 10: Basins of attraction for $K = 10^{-4}$, $\gamma = 10^{-4}$, and different values of e. The color code corresponds to the following attractors: quasi-periodic (black), 1/1 (purple), and 3/2 (yellow). The location for the SORs is marked with little green dots.

Table 2: Basin sizes and entropy for $\gamma = 10^{-4}$, $K = 10^{-4}$, and the eccentricities of the Moon and Mercury.

	Basin size			Entropy
e	1/1	3/2	Quasi-periodic	
e_{Moon}	22.13%		77.87%	0.529
$e_{Mercury}$	1.38%	1.17%	97.45%	0.136

resonance is painted purple, and the one for the 3/2 SOR is painted yellow. The basin sizes and the corresponding entropy are shown in Fig. 11. For $e = 0.0$, as expected, the synchronous resonance completely fills the phase space. For $e = 0.045$, a quasi-periodic orbit appears and its basin dominates the phase space. As the orbital eccentricity is increased, the basin of the 3/2 SOR steadily grows, until finally covering all the phase space at $e = 0.285$, where both the synchronous resonance and the quasi-periodic attractor disappear. After that, another quasi-periodic attractor appears along with its basin, which competes for space with the 3/2 SOR basin.

Fig. 11: Size of the basins of attraction for $K = 10^{-4}$ and $\gamma = 10^{-4}$, where QP stands for quasi-periodic attractors. The entropy is shown in red.

6 Conclusions

In this work, we have visually illustrated the basins of attraction for the dissipative spin-orbit problem, considering the parameters of Hyperion as a toy model, and the parameters for the Moon and Mercury. In all cases, the basins presented an intricate structure, being highly intertwined with one another.

The visual depiction of the system's complexity was complemented with the measure of the Gibbs entropy in each case, which takes into consideration the number of attractors, and was shown to be correlated to the dominant attractor in the system.

For Hyperion, the probability of a trajectory ending up in a synchronous rotation not only varies considerably as a function of the orbital eccentricity, but also the 1/1 SOR itself bifurcates and changes stability, rendering such final state impossible for e higher than a critical value. For the Moon and Mercury, where the equatorial oblateness is lower, quasi-periodic attractors appear and their basins of attraction act as barriers between the synchronous solution and the 3/2 SOR for values of e where the latter attractor exists.

In the future, we intend to use a more realistic rheological model (see, for example, Ragazzo and Ruiz 2017), and analyse how changes in the equatorial oblateness, which are due to long term variations of spin and tidal forces, might affect the topology of the basins of attraction. It is worth noticing that the Gibbs entropy investigated here can be easily extended to higher-dimensional physical models, which is important since we do not have access to tools for visually describing the system in this situation. Furthermore, we also found it to be a good criterion for convergence in Monte-Carlo simulations (see Appendix).

Data availability

The datasets generated and/or analysed during the current study are available from the corresponding author on reasonable request. The software used to generate and analyse said datasets was written by the authors and it is available at https://github.com/vitor-de-oliveira/spin-orbit.

Conflict of interest

The authors declare that they have no known competing financial interests or personal relationships that could have appeared to influence the work reported in this paper.

Acknowledgements

Appendix: Monte Carlo simulations for lower dissipation values

The dissipation constant sets the timescale for energy loss in the system, hence lower values of K means that orbits on the phase space take longer to converge on average, and computational time can become prohibitive in this situation. However, it is often possible to obtain results using Monte-Carlo simulations, since these require less initial conditions in order to measure a given quantity. In fact, we did compare our computations on the grid to Monte-Carlo simulations, for which we obtained similar results. A Monte-Carlo simulation is faster but the uniform grid method allows us to visually depict the basins of attraction, which was the focus of our work.
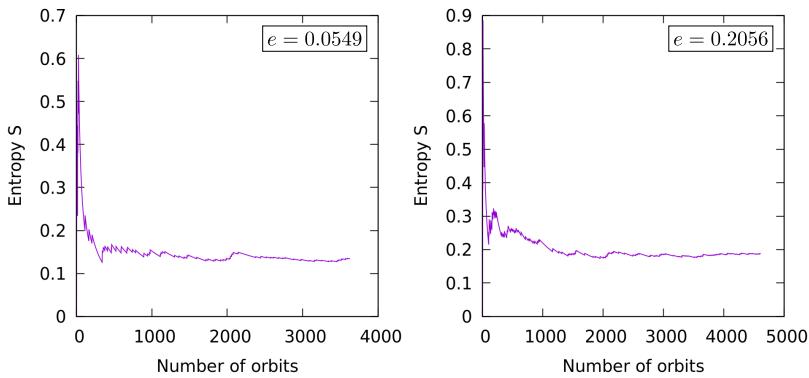
In Tables 3 and 4, we present the basin sizes and the entropy for values of K equal and lower than the one adopted in Sec. 5. In each simulation, we have selected up to 10^4 random initial conditions, evolved them in time, and used the entropy as a convergence criterion for the method (see Fig. 12). In the regime of lower values of the dissipation constant, there are more stable solutions whose basins compete for space. However, in almost all scenarios, the basins of attraction of quasi-period attractors almost completely dominated the observed region of the phase space.

Table 3: Basin sizes and entropy for $\gamma = 10^{-4}$ and $e = e_{Moon}$.

	Basin size				Entropy
K	1/1	3/2	Quasi-periodic	Other SORs	
10^{-4}	21.64%		78.36%		0.522
10^{-5}	0.91%	0.41%	98.68%		0.079
10^{-6}	0.85%	0.61%	97.91%	0.63%	0.124

Table 4: Basin sizes and entropy for $\gamma = 10^{-4}$ and $e = e_{Mercury}$.

	Basin size				Entropy
K	1/1	3/2	Quasi-periodic	Other SORs	
10^{-4}	1.21%	1.27%	97.52%		0.133
10^{-5}	0.94%	0.43%	98.28%	0.35%	0.132
10^{-6}	0.54%	0.65%	97.07%	1.74%	0.160

Fig. 12: Entropy as a function of the total number of randomly selected orbits for $\gamma = 10^{-4}$, $K = 10^{-6}$, (left) $e = e_{Moon}$, and (right) $e = e_{Mercury}$. The convergence of the measure S was used as a criterion for the convergence of the Monte-Carlo simulations.

References

Alexander JC, Yorke JA, You Z, Kan I (1992) Riddled basins. International Journal of Bifurcation and Chaos 2(04):795–813

Alligood KT, Sauer TD, Yorke JA (2012) Chaos: An Introduction to Dynamical Systems. Textbooks in Mathematical Sciences, Springer New York

Celletti A, Chierchia L (2008) Measures of basins of attraction in spin-orbit dynamics. Celestial Mechanics and Dynamical Astronomy 101:159–170

Celletti A, Chierchia L (2009) Quasi-periodic attractors in celestial mechanics. Archive for rational mechanics and analysis 191:311–345

Celletti A, Lhotka C (2014) Transient times, resonances and drifts of attractors in dissipative rotational dynamics. Communications in nonlinear science and numerical simulation 19(9):3399–3411

Correia AC, Boué G, Laskar J, Rodríguez A (2014) Deformation and tidal evolution of close-in planets and satellites using a maxwell viscoelastic rheology. Astronomy & Astrophysics 571:A50

Correia ACM, Delisle JB (2019) Spin-orbit coupling for close-in planets. Astronomy & Astrophysics 630:A102

Correia ACM, Laskar J (2004) Mercury's capture into the 3/2 spin-orbit resonance as a result of its chaotic dynamics. Nature 429(6994):848–850

Darwin GH (1879) I. On the bodily tides of viscous and semi-elastic spheroids, and on the ocean tides upon a yielding nucleus. Philosophical Transactions of the Royal Society of London (170):1–35

Daza A, Wagemakers A, Georgeot B, Guéry-Odelin D, Sanjuán MA (2016) Basin entropy: a new tool to analyze uncertainty in dynamical systems. Scientific reports 6(1):1–10

Daza A, Wagemakers A, Sanjuán MA (2022) Classifying basins of attraction using the basin entropy. Chaos, Solitons & Fractals 159:112,112

de Oliveira VM, Ciro D, Caldas IL (2020) Dynamical trapping in the area-preserving hénon map. The European Physical Journal Special Topics 229(8):1507–1516

Efroimsky M (2012) Bodily tides near spin–orbit resonances. Celestial Mechanics and Dynamical Astronomy 112(3):283–330

Efroimsky M, Lainey V (2007) Physics of bodily tides in terrestrial planets and the appropriate scales of dynamical evolution. Journal of Geophysical Research: Planets 112(E12)

Ferraz-Mello S (2013) Tidal synchronization of close-in satellites and exoplanets. a rheophysical approach. Celestial Mechanics and Dynamical Astronomy 116(2):109–140

Galassi M, Gough B, Rossi F, Theiler J, Jungman G, Booth M, Davies J (2001) GNU Scientific Library: Reference Manual. Network Theory Limited

Gibbs JW (2010) Elementary Principles in Statistical Mechanics: Developed with Especial Reference to the Rational Foundation of Thermodynamics. Cambridge Library Collection - Mathematics, Cambridge University Press, DOI 10.1017/CBO9780511686948

Goldreich P, Peale S (1966) Spin-orbit coupling in the solar system. The Astronomical Journal 71:425

Goldreich P, Re'em S (2009) Tidal evolution of rubble piles. The Astrophysical Journal 691(1):54

Henrard J (1985) Spin-orbit resonance and the adiabatic invariant. Resonances in the motion of planets, satellites and asteroids pp 19–26

Kokubo E, Ida S (2007) Formation of terrestrial planets from protoplanets. II. Statistics of planetary spin. The Astrophysical Journal 671(2):2082

Lichtenberg AJ, Lieberman MA (1992) Regular and chaotic dynamics. Applied mathematical sciences, Springer-Verlag

MacDonald GJF (1964) Tidal friction. Reviews of Geophysics 2(3):467–541

Mignard F (1979) The evolution of the lunar orbit revisited. I. The Moon and the planets 20(3):301–315

Murray CD, Dermott SF (1999) Solar System Dynamics. Cambridge University Press

Ott E (2002) Chaos in Dynamical Systems. Cambridge University Press

Peale SJ (2005) The free precession and libration of Mercury. Icarus 178(1):4–18

Pettengill G, Dyce R (1965) A radar determination of the rotation of the planet Mercury. Nature 206:1240

Ragazzo C, Ruiz LS (2017) Viscoelastic tides: models for use in Celestial Mechanics. Celestial Mechanics and Dynamical Astronomy 128(1):19–59

Raphaldini B, Ciro D, Medeiros ES, Massaroppe L, Trindade RIF (2020) Evidence for crisis-induced intermittency during geomagnetic superchron transitions. Physical Review E 101(2):022,206

Singer SF (1968) The origin of the moon and geophysical consequences. Geophysical Journal International 15(1-2):205–226

Wisdom J (1987a) Rotational dynamics of irregularly shaped natural satellites. The Astronomical Journal 94:1350–1360

Wisdom J (1987b) Urey prize lecture: Chaotic dynamics in the solar system. Icarus 72(2):241–275

Wisdom J, Peale SJ, Mignard F (1984) The chaotic rotation of hyperion. Icarus 58(2):137–152